Journal of Catalysis 428 (2023) 115134

Contents lists available at ScienceDirect

Journal of Catalysis

journal homepage: www.elsevier.com/locate/jcat

Research Article

The role of decarboxylation reactions during the initiation of the methanol-to-olefins process

Philipp Huber, Philipp N. Plessow *

Karlsruhe Institute of Technology, Institute of Catalysis Research and Technology, Hermann-von-Helmholtz-Platz 1, Eggenstein-Leopoldshafen, 76344, Germany

ARTICLE INFO

Keywords:
MTO
Zeolite
Initiation
Decarboxylation
Kinetic
Theory

ABSTRACT

The mechanism for direct C–C bond formation during the initiation of the methanol-to-olefins (MTO) process is still under discussion. Carbon dioxide formation is often observed during initiation, but there are only few investigations into the role of decarboxylation. We investigate decarboxylation pathways in the H-SSZ-13 zeolite from methanol to olefins via direct carbon–carbon coupling. Additionally, the rate-determining steps were recomputed in the H-ZSM-5 and H-SAPO-34 zeolite. Gibbs free energy barriers were calculated using periodic density functional theory in combination with CCSD(T) calculations on cluster models. For H-SSZ-13, kinetic batch reactor simulations were performed. We found for H-SSZ-13 that pathways via decarboxylation reactions are equally likely as previously computed pathways including decarbonylation mechanisms (also known as ketene or CO pathway). Lactones formed from ketenes and formaldehyde were identified as the main intermediates. The decarboxylation mechanism has similar barriers in H-SSZ-13, H-ZSM-5, and H-SAPO-34, while the barriers for methylation and decarbonylation reactions are significantly lower in H-ZSM-5 and higher in H-SAPO-34. Decarboxylation reactions of lactones could explain experimentally detected carbon dioxide during the initial phase of the MTO process.

1. Introduction

The zeolite-catalyzed methanol-to-olefins (MTO) process converts methanol to light olefins [1,2]. Since methanol can be obtained from renewable resources, like biomass [3–6] and carbon dioxide [7,8] captured from industrial processes or air [9–12], this process provides a sustainable alternative to the utilization of crude oil. In the MTO process, olefins are formed from methanol catalytically [13,14], which requires the presence of the hydrocarbon pool (HCP) as co-catalyst. While these hydrocarbons could be introduced as impurities [15,16], the first olefins can also be formed via direct C–C coupling from methanol [17]. The mechanism of this direct formation of olefins is not completely understood and still subject of recent investigations [18–24]. Some intermediates formed during the initiation of the MTO process were also proposed to play a crucial role during deactivation processes in zeolites [20]. Many initiation mechanisms for the MTO process have been suggested [1,25,26]. The most important ones are explained below: In the oxonium ylide mechanism [27], dimethyl ether (DME) and surface methoxy species (SMS) form a trimethyl oxonium ion, which can be deprotonated to an ylide. This ylide reacts intermolecularly with a second SMS or intramolecularly via Stevens-type rearrangement to ethylmethyl ether which afterwards decomposes to ethene and methanol. During the carbene mechanism, CH_2 is formed from methanol [28–30]. Carbenes can then polymerize or react with methanol or DME. In a proposed radical mechanism, permanent localized surface radicals initialize the formation of methyl and methylmethoxy radicals which couple and react to olefins [31] Tajima et al. proposed the methane–formaldehyde mechanism describing the reaction of CH_4 and formaldehyde (FA) to ethanol, which further dehydrates to ethene [32]. Similar mechanisms exist, which involve for example methanol or DME as a reactant instead of CH_4 [33,34]. In a ketene-mediated mechanism (also called CO catalyzed mechanism), CO reacts with SMS to ketene, which is further methylated and decarbonylated to olefins [35]. Decarbonylation reactions of ketenes have also been discussed in related mechanism as in the guaiacol pyrolysis [36].

The ketene mechanism as computed previously [19,37] is sketched in Fig. 1 and described in the following. First, methanol is converted to SMS and DME. The reactivity of SMS in zeolites including its role for the MTO process is a broadly investigated area [17,38]. The formation of DME proceeds via a dissociative (mediated by a SMS) or an associative mechanism [39–46]. FA is formed from methanol or DME through a hydrogen transfer (HT). Reaction of methanol with a SMS yields CH_4 as a side product, while reaction with the Brønsted acid site releases FA and H_2. Similarly, DME can react through a HT with a SMS or with the acidic proton from the zeolite to a zeolite

* Corresponding author.
E-mail address: philipp.plessow@kit.edu (P.N. Plessow).

https://doi.org/10.1016/j.jcat.2023.115134
Received 11 July 2023; Received in revised form 18 September 2023; Accepted 20 September 2023
Available online 29 September 2023

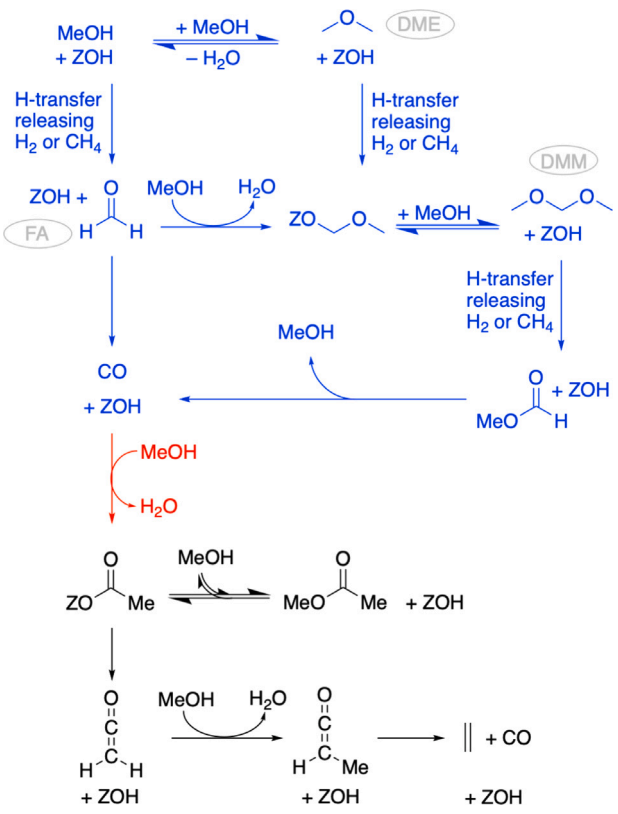

Fig. 1. Ketene mechanism via decarbonylation (simplified). Blue — formation of CO, red — C–C coupling via CO and SMS, black — decarbonylation to ethene. Abbreviations used for adsorbates are added in gray. Hydrogen transfer reactions between educts and the proton of the zeolite Brønsted acid site yielding H_2 or a methylation agent (MeOH, DME, SMS) yielding CH_4 were considered.

surface methoxymethyl, also releasing CH_4 or H_2, respectively. The surface methoxymethyl group can also be formed through reaction of FA with a SMS. Dimethoxymethane (DMM) formed from a surface methoxymethyl group and methanol can react further via HT reactions to methylformate eventually releasing CH_4 or H_2 again. Methylformate decomposes to carbon monoxide and methanol. FA can also react to carbon monoxide and H_2 via HT reactions. Reaction of CO with a SMS gives a zeolite surface acetate, where the first C–C bond is formed. This surface acetate can react with methanol to a methyl acetate or dissociate from the surface, yielding a ketene. Ketene can be methylated to methyl ketene, which can decarbonylate to ethene. Methyl ketene can also be further methylated and decarbonylated to propene and isobutene (not depicted in Fig. 1).

Although it is difficult to detect reactive intermediates in zeolites [47], many important intermediates of the CO initiation mechanism discussed above have been observed during the MTO process. SMS [48–54], DME [41,55,56], and FA [20,57,58] have been detected in multiple studies and are commonly accepted intermediates. DMM, zeolite surface acetate, and methyl acetate have been detected in H-SAPO-34 [24]. While surface methoxymethyl groups have not been detected yet, the hydrolyzed product of DMM, methanediol, has been identified [24]. In contrast, CO has been frequently observed during the MTO process [20,59,60]. In $ZnAlO_x$/H-ZSM-5, surface acetate and formate have been detected after conversion of syngas [61]. A zeolite surface acetate was also observed from conversion of SMS and CO in H-MOR [62]. In H-ZSM-5, methyl acetate and surface acetate have been detected during methanol conversion [22]. Methylacetate was also detected using methylal as feed in H-ZSM-5 [63]. Conversion of CO/DME/D_2O in H-MOR was conducted to identify ketene via H_2DCOOD [64]. Ketene was also identified in H-MOR from conversion of CH_3COCl [23]. Recently, methyl ketene was detected during conversion of methylacetate in H-ZSM-5 [21]. Methane was often detected [20,57,65–67] and hydrogen was also observed [22], however, in another study, formation of hydrogen is reported to be insignificant [66].

Carbon dioxide was also observed experimentally during the initiation of the MTO process [13,20,57,59,60,67] which cannot be explained with the mechanisms discussed above. In principle, CO_2 could also result from the reaction of the produced CO via the water gas shift reaction. While zeolites cannot catalyze the water gas shift reaction [66], Chen et al. claimed the stainless steel reactor to catalyze this reaction during the MTO process [68]. The Lercher group proposed two mechanisms for the zeolite-catalyzed formation of carbon dioxide. First, they suggested a ketonic decarboxylation of acetic acid [63]. However, we found this mechanism, including the coupling of two C2 species, to be unlikely in a computational study using the H-SSZ-13 zeolite [69]. The second proposed mechanism comprises the formation and decarboxylation of acrylic acid, which was detected via IR [20]. For this, they proposed the reaction of FA with a ketene derivative. They also discussed the role of FA for the deactivation of the zeolite catalyst and proposed a mechanism involving the reaction of FA with a zeolite surface acrylate [70].

In this work, we investigate the role of decarboxylation reactions during the initiation of the MTO process computationally. We consider acrylic acid as well as lactones, which can also be formed from ketene and FA, as intermediates. These species can decarboxylate to olefins, which enter the autocatalytic olefin cycle. We compare these decarboxylation mechanisms with the ketene-mediated mechanism computed previously, where olefins are formed through decarbonylation of ketenes [19,37].

2. Computational details

We investigated the H-SSZ-13, H-SAPO-34, which crystallize in the chabazite framework, and H-ZSM-5 zeolite, which crystallizes in the MFI framework. While the chabazite structure has only one unique T-site, H-ZSM-5 has twelve T-sites of which we considered the T12-site. For all zeolites, we used models with one active site per unit cell. For H-SSZ-13 and H-SAPO-34, which are isoelectronic, this leads to a Si/Al ratio and an (Al+P)/Si ratio, respectively, of 35. The lattice constants are $a = b = 13.625$ Å and $b = 15.067$ Å for H-SSZ-13 and $a = b = 13.875$ Å and $b = 15.017$ Å as used in previous studies [19,71]. For H-ZSM-5, the Si/Al ratio is 96 and lattice constants are $a = 20.340$ Å, $b = 19.988$ Å and $b = 13.492$ Å as used earlier [71]. The 46 T-site and 52 T-site cluster models for the chabazite and MFI framework, respectively, were cut from periodic structures, where terminal Si-O was replaced with Si-H groups pointing in the same direction with a fixed bond length of 1.489 Å. All structures were optimized in periodic density functional theory (DFT) calculations using the PBE-D3 [72,73] functional with a convergence criterion of 0.001 eV $Å^{-1}$ for the atomic forces. The automated relaxed potential surface scans (ARPESS) [74], nudge elastic bond (NEB) [75], and dimer [76] method were used to search for transition states. Transition states were verified to have only a single imaginary frequency along which the transition state was distorted and optimized to determine reactant and product structures. The oxygen atoms at which the reactions occur are listed in Table S10. Gibbs free energies were computed at 400 °C. For the contribution of vibrations, the harmonic oscillator approximation was used where frequencies below 12 cm^{-1} were increased to this value to reduce errors of the harmonic approximation [77]. A partial Hessian was used for adsorbed structures considering the adsorbed molecule, the Al atom, and the four adjacent Si-O groups only. For gaseous molecules, translational and rotational degrees of freedom were considered additionally within the free-translator and rigid-rotator approximation. Since DFT at the GGA-level underestimates barriers [78], we employ ab initio calculations on cluster models, an approach that was pioneered by the group of

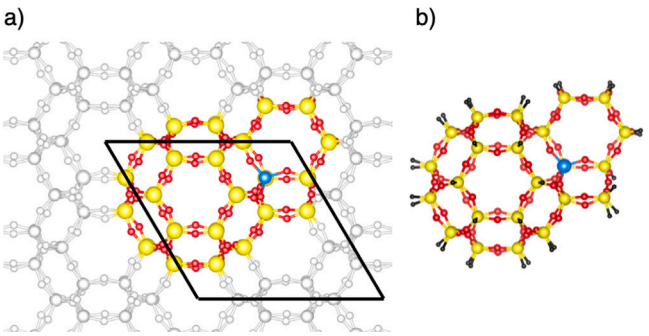

Fig. 2. (a) Periodic and (b) cluster-model structure of H-SSZ-13. The unit cell of the periodic structure is indicated with black lines and the part cut for the cluster model is colored while the remaining framework is depicted in gray. Color code: Al — blue, Si — yellow, O — red, H — black, C — brown, remaining framework — gray.

Joachim Sauer [79]. We performed single-point calculations on cluster models to obtain a correction term ΔE^{CM} (see Eqs. (1) and (2)):

$$G = E^{PBC}_{PBE-D3} + \Delta E^{CM} + \Delta G^{PBC}_{harm} \quad (1)$$

$$\Delta E^{CM} = E^{CM}_{DLPNO-CCSD(T)/DZ} + \Delta E^{CM}_{MP2/CBS} - E^{CM}_{PBE-D3} \quad (2)$$

Here, G is the cluster-model corrected Gibbs free energy, E^{PBC}_{PBE-D3} is the periodic DFT energy, and ΔG^{PBC}_{harm} is the Gibbs free energy contribution at 400 °C and 1 bar. $E^{CM}_{DLPNO-CCSD(T)/DZ}$ is the DLPNO-CCSD(T) [80] energy with the cc-pVDZ [81] basis set and E^{CM}_{PBE-D3} is the DFT energy of cluster models using the def2-TZVPP [82] basis set. $\Delta E^{CM}_{MP2/CBS}$ is a correction term for a complete basis set (CBS) extrapolation carried out separately for the Hartree Fock (HF) and the MP2 limit. The three-point exponential fit [83] with the cc-pVXZ [81] basis sets (X = D, T, Q) was used for the HF limit and the two-point X^{-3} fit [84] with the cc-pVXZ basis sets (X = D, T) was used for the MP2 limit. Periodic DFT calculations were carried out with the Vienna Ab Initio Simulation Package (VASP, version 5.4.1.) [85–89] using an energy cutoff of 400 eV. The atomic simulation environment was employed [90]. The ORCA program package [91] was used for HF, MP2, and CCSD(T) calculations. The DLPNO approximation [80] and the "TightPNO" setting were employed for the correlation methods. For HF calculations, the RIJCOSX approximation [92] using the X6 grid was applied. DFT calculations on cluster models were performed with the Turbomole program package [93] using the resolution of identity approximation [94].

3. Results and discussion

Gibbs free energy profiles for H-SSZ-13

We investigated several mechanisms for the coupling of formaldehyde with acetic acid derivatives, which yields acrylic acid. For these derivatives, acetic acid, 1,1-dihydroxyethene, and ketene were considered.

Structures were optimized with periodic DFT using the PBE-D3 functional and a correction term was added to the DFT energy at the CCSD(T) level of theory obtained from single-point calculations at 46T cluster models. The periodic and cluster-model structure of H-SSZ-13 are shown in Fig. 2. Gibbs free energies were calculated at 400 °C. The energetic span model [95] was used to calculate energy barriers. Adsorbed and gaseous states have been considered for all species and the state with lower Gibbs free energy is considered.

The most favorable path for the formation of acrylic acid is the reaction of a ketene with a FA to propiolactone (see Figs. S2 and S3), which can react further to acrylic acid with a zeolite bound species as an intermediate. The rate-determining barrier is $\Delta G^{\ddagger}$ = 205 kJ/mol referenced to gaseous methyl acetate, FA, and the empty zeolite. Methyl acetate can easily be formed from ketene (via surface acetate) and has a 51 kJ/mol lower free energy. The decarboxylation of acrylic acid to ethene has a higher barrier of $\Delta G^{\ddagger}$ = 236 kJ/mol (referenced to adsorbed acrylic acid, see Fig. S2). We also investigated the direct decarboxylation of propiolactone which has a lower barrier of $\Delta G^{\ddagger}$ = 217 kJ/mol (referenced to adsorbed acrylic acid). Thus, decarboxylation via propiolactone is more likely than via acrylic acid. However, formation of acrylic acid has a lower barrier than decarboxylation of propiolactone which explains the observed acrylic acid during the initiation of the MTO process [20]. For the decomposition of propiolactone in the gas phase, a free energy barrier of 157 kJ/mol was determined experimentally at 400 °C [96]. Referenced to propiolactone, we obtain a barrier of 165 kJ/mol, which is thus in very good agreement.

We further investigated decarboxylation mechanisms via lactones and compared these to the previously computed decarbonylation mechanism [19]. In Fig. 3a, both the decarboxylation and decarbonylation mechanism are depicted. Ketene can be further methylated to methyl ketene, dimethyl ketene, and a pivaloyl cation. As conversions between ketene, acylium cations, and zeolite surface esters have low barriers, these reactions are equilibrated fast. For clarity, only one of these species is depicted in Fig. 3; however, all can be formed easily (see SI). Methyl ketene, dimethyl ketene, and the pivaloyl cation can be decarbonylated yielding CO and ethene, propene, and isobutene, respectively. Structures of methylation and decarbonylation reactions have been taken and recomputed from previous work [19]. Ketene, methyl ketene, and dimethyl ketene can also couple with FA to lactones (propiolactone, 3-methyloxetan-2-one, and pivalolactone). These lactones can decarboxylate to CO_2 and ethene, propene, and isobutene, respectively. When comparing decarboxylation and decarbonylation, an important distinction is that for the formation of a specific olefin, decarbonylation requires one more methylation step. For example, decarbonylation of methyl ketene gives ethene, while its reaction with formaldehyde and subsequent decarboxylation gives propene. The ketene species can also easily react to methyl esters (see Fig. 3b) with all barriers ≤ 114 kJ/mol. Since these esters have low Gibbs free energies, they have to be considered as the reference states when calculating barriers within the energetic span model [95]. For methyl pivalate (ME4), the situation is different, because of the extremely low barrier for decarbonylation (76 kJ/mol relative to K4), which is lower than the barrier for the formation of the methyl ester (110 kJ/mol). For the sake of consistency, we have nevertheless referenced the barriers for decarbonylation of K4 to ME4 in both Fig. 3d) and Table 2 with a value of 140 kJ/mol. The computed reactions from ketenes to methyl esters proceed in several steps. Ketenes become protonated to acylium cations and react to zeolite surface esters. These esters react with methanol to methyl esters (see SI). In Fig. 3c, the transition states are depicted for the C–C coupling of ketene with FA, the decarboxylation of propiolactone, the methylation of ketene, and the decarbonylation of methyl ketene. These transition states are exemplary for analogous transition states of higher methylated species. The corresponding Gibbs free energy diagram of the initiation mechanism is shown in Fig. 3d, where the decarboxylation and decarbonylation barriers are compared.

The barriers shown in Fig. 3d are often relatively similar, with no obvious preference for the reactivity of the ketenes. Generally, the reactions with formaldehyde preceding the decarboxylation reactions only require low barriers and will thus be discussed separately. Starting from ketene, decarboxylation to ethene requires a barrier of 213 kJ/mol, while further methylation occurs with a barrier of 216 kJ/mol. Methyl ketene can either be methylated ($\Delta G^{\ddagger}$ = 207 kJ/mol), decarbonylated to ethene ($\Delta G^{\ddagger}$ = 214 kJ/mol) or decarboxylated to propene ($\Delta G^{\ddagger}$ = 199 kJ/mol). Finally, methylation of dimethyl ketene ($\Delta G^{\ddagger}$ = 182 kJ/mol), its decarbonylation ($\Delta G^{\ddagger}$ = 170 kJ/mol) or its decarboxylation ($\Delta G^{\ddagger}$ = 182 kJ/mol) are again relatively similar. The decarbonylation of the pivalyl cation requires only a low barrier of 140 kJ/mol relative to the ester ME4 and, as discussed above, of 76 kJ/mol relative to K4. In general, the decarboxylation mechanism is slightly more

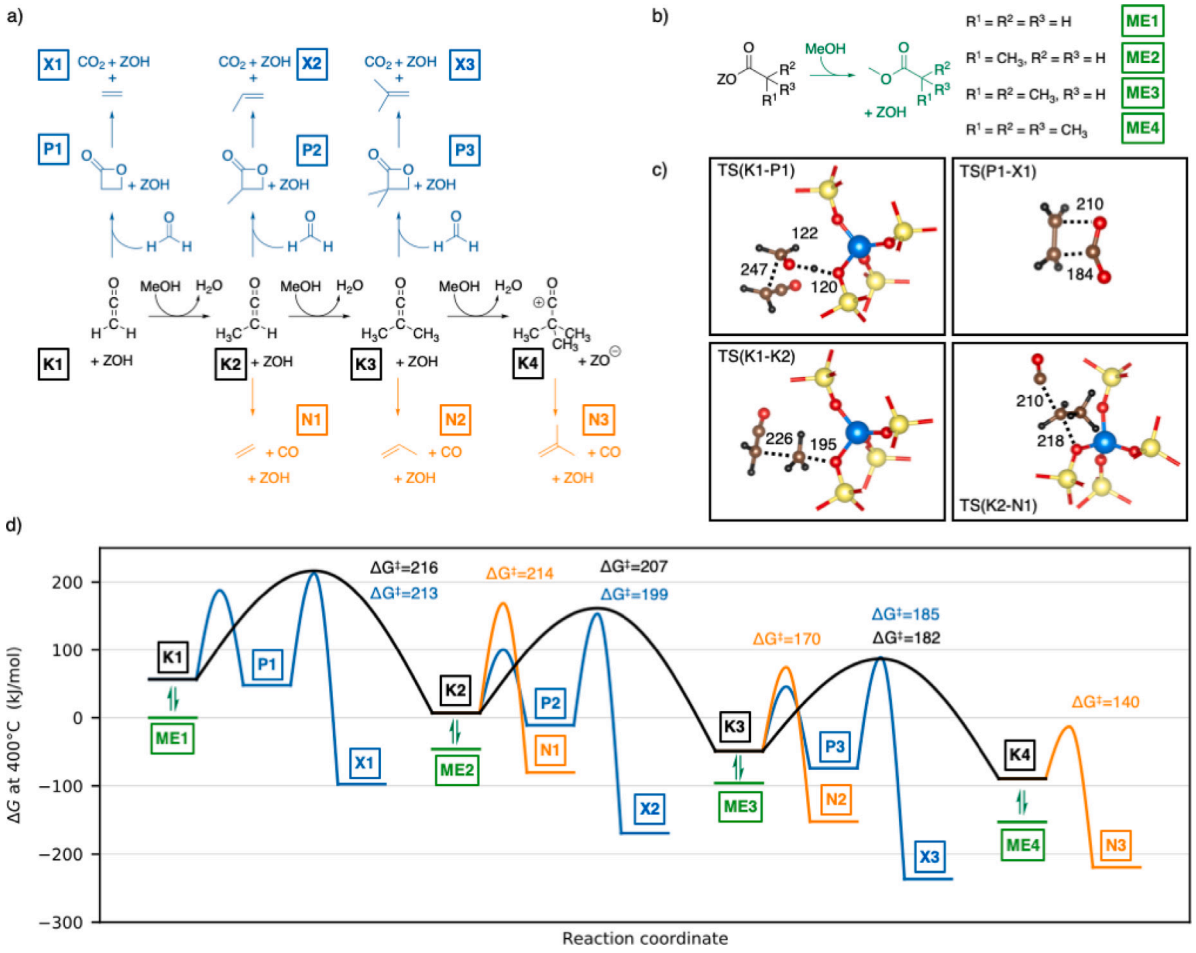

Fig. 3. (a) Mechanism for the initiation of the MTO process via decarboxylation reactions of lactones and decarbonylation reactions of ketenes. (b) Formation of methyl esters. (c) Atomic structure of transition states. Atomic distances are given in pm. (d) Corresponding Gibbs free energy diagram at 400 °C. Reference state at 0 kJ/mol is methyl acetate. Methylation (black), decarboxylation (blue), decarbonylation (orange), and methyl esters (green).

favorable than the decarbonylation mechanism when referring to Gibbs free energy barriers.

Next, we discuss the reaction mechanisms in more detail. For the formation and decarboxylation of lactones, several barriers have been calculated. The ketenes can react with FA in either a direct or a step-wise mechanism. The direct lactone formation as well as the decarboxylation reactions can proceed catalyzed by the zeolite or uncatalyzed in the gas phase. The lowest barriers are depicted in Fig. 3d. Table 1 lists all barriers for these lactone-related reactions. For the step-wise lactone formation, first a C–C bond is formed while the oxygen of FA becomes protonated (see structure TS(K1-P1) in Fig. 3c). Secondly, the ring closes and the oxygen is deprotonated again. For P1 and P2, the direct catalyzed mechanism is initialized by a bond formation of the electrophilic carbon atom of the ketene and the oxygen of FA. The C–C bond is formed afterwards without an additional barrier. For P3, the direct catalyzed mechanism is initialized by a C–C bond formation resembling the step-wise mechanism. This is also reflected by a barrier more similar to the barriers of the other step-wise than to the direct mechanisms. The direct mechanisms in the gas phase proceed through concerted formation of C–C and C–O bonds. The decarboxylation reactions initialized by C–O bond cleavage have higher barriers than the formation of lactones. For P1 and P2, this reaction is more favorable in the gas phase due to entropy (see structure TS(P1-X1) in Fig. 3c); for P3, it is more favorable when catalyzed by the zeolite due to increasing dispersion energies for larger molecules in the adsorbed state. As shown in Table S9, starting from the lactones, the contribution of entropy to activation barriers ($-T\Delta S^{\ddagger}$) is below 10 kJ/mol in the gas phase, while it is > 100 kJ/mol for the transition states in the zeolite. Conversely, the activation enthalpy is about 100 kJ/mol higher for the gas phase so that the activation Gibbs free energies are eventually in the same range.

Table 1
Barriers for step-wise and direct lactone formation as well as lactone decarboxylation. For the latter, barriers for uncatalyzed and catalyzed states were computed. Barriers in kJ/mol referenced to the previous most stable state (previous methyl ester) at 400 °C. Bold values are used in Fig. 3d.

Reaction \ intermediate	P1	P2	P3
Step-wise formation TS1	**188**	**146**	159
Step-wise formation TS2	149	114	113
Direct formation catalyzed	296	276	**142**
Direct formation gas phase	273	278	267
Decarboxylation catalyzed	231	203	**185**
Decarboxylation gas phase	**213**	**199**	188

The methylation reactions of ketenes proceed via SMS (see structure TS(K1-K2) in Fig. 3c) and yield the corresponding acylium cation. For K1, K2, and K3, the free energies of the ketenes are depicted in Fig. 3d, while for K4, the free energy of the zeolite surface ester is shown. Decarbonylation reactions to olefins start from the zeolite surface esters, not from the ketene. The transition state TS(K2-N1) (see Fig. 3c) actually yields a zeolite ethoxy group. The elimination from the zeolite to ethene has a low barrier of $\Delta G^{\ddagger} = 152\,\mathrm{kJ/mol}$ compared to the formation of the ethoxy group with $\Delta G^{\ddagger} = 214\,\mathrm{kJ/mol}$.

We additionally calculated a deactivation pathway comprising the coupling of FA and acrylic acid to 2(5H)-furanone, which further reacts

with ethene to phenole (see SI). A similar mechanism was proposed by Müller et al. [70]. However, with a barrier of 285 kJ/mol for the reaction of FA with acrylic acid, this pathway is unlikely. Ketene could also dimerize and decarboxylate to isobutene in principle via several pathways, which we investigated previously [69]. Here, we additionally computed the coupling of two ketenes (as well as coupling of methylated ketene species) and further decarboxylation reactions to cumulenes. However, these reactions are unfavorable, due to their high barriers (>250 kJ/mol, see SI).

Comparing barriers is a straightforward approach to discussing the relevance of reaction mechanisms, however, it does not capture all aspects. During the initiation of the MTO process, FA is present in significantly lower concentration than methanol. This makes the decarboxylation mechanism involving the reaction of ketene with FA inherently less favorable. In contrast, the decarbonylation mechanism does not require FA but methanol for the reaction with ketene. This issue can be addressed in a kinetic simulation, where concentrations are explicitly taken into account.

Kinetic modeling for H-SSZ-13

For a quantitative analysis of the above discussed reaction mechanism, we applied kinetic batch reactor simulations at 400 °C. We assumed perfect mixing in our reactor model and used an active site concentration of 17.9 mol/m^3 as in previous work [37]. For the kinetic models, we considered (i) barriers computed for the initiation from methanol to surface acetate [19], (ii) barriers discussed in this work, i.e., decarboxylation mechanisms via acrylic acid and lactones and decarbonylation mechanisms, and (iii) barriers for methylation and cracking reactions [97] within the autocatalytic cycle after the initiation. Barriers taken from other studies [19,97] applied correction terms for cluster models at the MP2 level of theory. The difference to DLPNO-CCSD(T) used in this work was found to be less than 10 kJ/mol on average [78]. The simulated pressures of methanol, water, DME, and olefins are shown in Fig. 4a and the pressures of carbon monoxide, carbon dioxide, and FA are shown in Fig. 4b. Methanol is consumed, water is formed, and after a certain light-off time, the olefin pressure raises rapidly. The pressures of carbon monoxide, carbon dioxide, and FA are low during the whole simulation. We define the initiation time as the time when olefins reach a pressure of 0.005 bar. To compare the above discussed initiation mechanisms, kinetic simulations were carried out by considering only one of these mechanisms, i.e., either the mechanism involving the decarbonylation of ketenes (M1), the mechanisms involving the decarboxylation of acrylic acid (M2), or the mechanism involving the decarboxylation of lactones (M3). Additionally, a simulation with all three mechanism was performed (also see Fig. 4). The initiation time considering all mechanisms is 8.72 s. While M1 and M3 have comparable initiation times of 8.80 s and 8.87 s, respectively, M2 has a significantly longer initiation time of 10.64 s. Thus, the decarboxylation of acrylic acid is unlikely to be responsible for experimentally observed carbon dioxide. The formation and decarboxylation of lactones, in contrast, might explain the CO_2 formation.

As discussed in Ref. [37], the amount of olefins formed directly by initiation is very low and the observable amount of olefins is formed mainly by the HCP. The pressure of FA formed during our simulation is significantly lower than in experiments. The maximum pressure up to the initiation time is $1.69 \cdot 10^{-4}$ bar. This corresponds to a selectivity of 0.17% to FA during the initiation time, while 86.64% of methanol is consumed. In experiments with H-ZSM-5, selectivities up to several percentage points were observed at low methanol conversions [20,65]. For instance, in H-ZSM-5, a MeOH/DME conversion of 0.24% yielded a FA selectivity of 25% at 475 °C [20]. However, we computed a FA selectivity of $4 \cdot 10^{-5}$% at a methanol conversion of 0.25%.

To discuss the reaction mechanisms at more realistic FA pressures, we performed additional kinetic simulations, where we used different

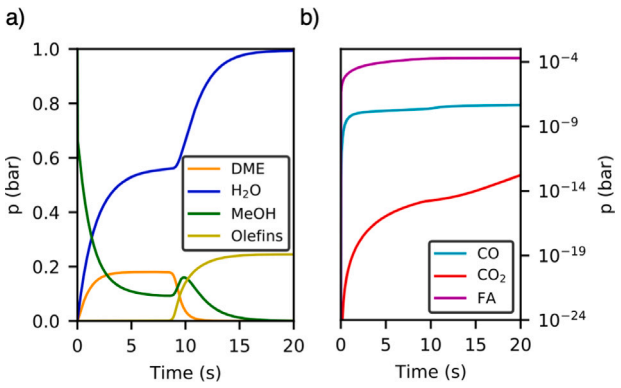

Fig. 4. Kinetic batch reactor simulations at 400 °C. All three initiation mechanisms and reactions within the autocatalytic olefin cycle are considered. Pressures of water, methanol, and olefins (a) and pressures (logarithmic scale) of carbon monoxide, carbon dioxide, and formaldehyde are given (b).

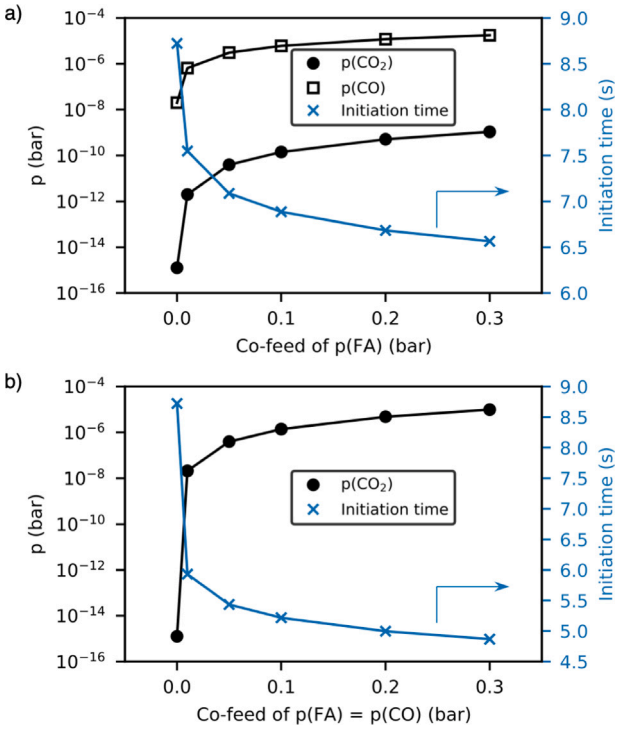

Fig. 5. Varying FA pressures (a) and varying pressures of FA and CO with p(FA) = p(CO) (b) as co-feed to 1 bar methanol at 400 °C. For both figures, co-feeds of p(FA) of 0.00 bar, 0.01 bar, 0.05 bar, 0.10 bar, 0.20 bar, 0.30 bar have been used. Pressures of carbon monoxide and carbon dioxide are given at the initiation time.

pressures of FA as a co-feed to 1 bar methanol. Fig. 5a shows that the initiation time is reduced from 8.72 s to 6.56 s for a co-feed of 0.3 bar FA. The pressure of CO_2 increases more strongly than the pressure of CO for larger FA pressures. It is noteworthy, that the activity of decarbonylation and decarboxylation for initiation cannot be compared based on CO and CO_2-formation. This is because CO is only catalytic, i.e. each ketene is formed from CO and decarbonylation only results in the formation of the same amount of CO already present. CO_2-formation, on the other hand, is a dead-end, at least in our kinetics so it is a direct measure of decarboxylation activity. For a FA co-feed of 0.3 bar, olefins of $1 \cdot 10^{-9}$ bar are formed through decarboxylation of lactones while only $4 \cdot 10^{-13}$ bar are formed through decarbonylation of ketenes up to the initiation time. Thus, higher FA pressures clearly favor the decarboxylation pathway.

Not only the FA pressure but also the CO pressure is underestimated by our kinetic simulation (all considered mechanisms for FA- and CO-formation are shown in Fig. S9). In another experimental study [67], DME was converted in H-ZSM-5 at 475 °C to about 0.08% CO, 0.02% CO_2, and 0.06% FA at a low contact time with a DME conversion < 0.3%. For comparison, we performed a simulation with 1 bar DME instead of methanol as feedstock, but no CO_2 was formed at a DME conversion of 0.33%. To mimic the experimental conditions, we used 0.08% CO and 0.06% FA as a co-feed to DME, where $2 \cdot 10^{-18}$ and $1 \cdot 10^{-10}$ CO_2 were formed after a DME conversion of 0.33% and up to the initiation time (3.17 s), respectively. Fig. 5b shows the pressures of CO_2 formed up to the initiation time when using different pressures of co-feed for CO and FA to MeOH in a kinetic simulation with p(FA) = p(CO). The CO_2 pressure increases to $2 \cdot 10^{-8}$ bar for a co-feed of p(CO) = p(FA) = 0.01 bar Overall, the amount of CO_2 formed in our simulations is lower than reported in experiments [13,20,67]. This is at least partially due to the fact that the precursors, CO and FA, are already formed in much lower amounts.

Comparison to H-ZSM-5 and H-SAPO-34

We chose the H-SSZ-13 zeolite as catalyst for our investigation, primarily due to its structural simplicity and computational efficiency since it has a small unit cell and only one unique T-site. For industrial application, other zeotypes like H-ZSM-5 or H-SAPO-34, are more relevant. H-ZSM-5 has a larger unit cell and twelve T-sites, of which we considered only the T12 site. The periodic structure and the cluster model of H-ZSM-5 are depicted in Fig. S4. H-SAPO-34 has the same framework as H-SSZ-13 (with one unique T-site), but is an aluminophosphate substituted with a silicon atom at the active center. We studied the discussed mechanism for the H-ZSM-5 and H-SAPO-34 zeolite, but considered only the rate-determining reaction steps (see Table 2). In most cases, decarboxylation is most favorable in the gas phase, leading to identical activation barriers, except for dimethyl ketene where TS(P3-X3) is in H-SSZ-13 and H-SAPO-34 slightly more favorable when occurring in the zeolite. Uncatalyzed decarboxylation reaction are generally preferred entropically since the transition state has three translation and three rotational degrees of freedom. Catalyzed reactions benefit from dispersion interaction with the framework and of course from the interaction with the acidic proton. The uncatalyzed reactions encountered in this work are a somewhat rare case, since they can proceed without an acid catalyst, which is typically not the case for most zeolite-catalyzed reactions, such as methylation reactions.

Compared to H-SSZ-13, the barriers for methylation and decarbonylation are about 10 to 20 kJ/mol lower in H-ZSM-5 and about 10 to 20 kJ/mol higher in H-SAPO-34. As shown in the parity plots in Fig. S5, the difference in decarbonylation barriers is already present at the PBE-D3 level of theory, but slightly increases when applying the cluster corrections. Thus, when evaluating free energy barriers, the decarbonylation mechanism is more favorable in H-ZSM-5 than in H-SSZ-13, while in H-SAPO-34 the decarboxylation mechanism is more favorable than in H-SSZ-13.

4. Conclusion

MTO initiation pathways in the H-SSZ-13 zeolite were investigated computationally. We found a decarboxylation mechanism via lactones to be reasonable with a barrier of $\Delta G^{\ddagger} = 213$ kJ/mol for the decarboxylation of propiolactone. The rate-determining step for a previously computed decarbonylation mechanism has a similar barrier of $\Delta G^{\ddagger} = 216$ kJ/mol. Thus, both mechanisms are likely and CO as well as CO_2 can be formed together with olefins. Based on the computed free energy barriers, kinetic batch reactor simulations were performed. We found that both decarboxylation of lactones and decarbonylation of ketenes are similar in activity for initiation. Formation of CO_2 during the initiation of the MTO process could thus be due to the decarboxylation of lactones formed from the coupling of ketenes and formaldehyde. However, quantitative agreement with experiments is not reached, since our simulations generally predict too low CO_2 pressures. This is to some extent due to too low CO- and formaldehyde-pressures, as simulations with co-feeds of these gases show.

In addition to H-SSZ-13, free energy barriers were computed for the rate-determining steps in H-ZSM-5 and H-SAPO-34. The barriers for decarboxylation reactions are similar in all three zeotypes, while barriers for methylation and decarbonylation reactions are somewhat lower in H-ZSM-5 and higher in H-SAPO-34 compared to H-SSZ-13.

Table 2
Rate-determining reaction barriers in H-ZSM-5, H-SAPO-34, and H-SSZ-13. The barriers are referenced to the corresponding methyl ester. All barriers are given at 400 °C in kJ/mol. For decarboxylation reactions, the uncatalyzed gas phase reaction barrier is lower in most cases, and is the one listed if that is the cases. All decarboxylation barriers are listed in the SI.

Reaction	Reactant	H-ZSM-5	H-SAPO-34	H-SSZ-13
Methylation of ketenes				
TS(K1-K2)	($OCCH_2$)	202	232	216
TS(K2-K3)	($OCCHCH_3$)	181	218	207
TS(K3-K4)	($OCC(CH_3)_2$)	167	202	182
Decarboxylation of lactones				
TS(P1-X1)	(OC_3H_4)	213[a]	213[a]	213[a]
TS(P2-X2)	($OC_3H_3CH_3$)	199[a]	199[a]	199[a]
TS(P3-X3)	($OC_3H_3(CH_3)_2$)	188[a]	187	185
Decarbonylation of ketenes				
TS(K2-N1)	($OCCHCH_3$)	190	236	214
TS(K3-N2)	($OCC(CH_3)_2$)	146	187	170
TS(K4-N3)	($OCC(CH_3)_3^+$)	118	163	140

[a] Barriers for uncatalyzed gas phase reactions.

Declaration of competing interest

The authors declare the following financial interests/personal relationships which may be considered as potential competing interests: Philipp N. Plessow reports financial support was provided by Karlsruhe Institute of Technology North Campus.

Data availability

All relevant data is provided as SI.

Acknowledgments

The authors acknowledge support by the state of Baden-Württemberg through bwHPC (bwunicluster and JUSTUS, RV bw17D011) and the German Research Foundation (DFG) through grant no INST 40/575-1 FUGG (JUSTUS 2 cluster). Financial support from the Helmholtz Association, Germany is also gratefully acknowledged. Gefördert durch die Deutsche Forschungsgemeinschaft (DFG) Projektnummer 434253773.

Appendix A. Supplementary material

Supplementary material related to this article can be found online at https://doi.org/10.1016/j.jcat.2023.115134.

References

[1] M. Stöcker, Methanol-to-hydrocarbons: Catalytic materials and their behavior, Microporous Mesoporous Mater. 29 (1–2) (1999) 3–48.
[2] U. Olsbye, S. Svelle, M. Bjørgen, P. Beato, T.V. Janssens, F. Joensen, S. Bordiga, K.P. Lillerud, Conversion of methanol to hydrocarbons: How zeolite cavity and pore size controls product selectivity, Angew. Chem. Int. Edn 51 (24) (2012) 5810–5831.
[3] A. Corma, S. Iborra, A. Velty, Chemical routes for the transformation of biomass into chemicals, Chem. Rev. 107 (6) (2007) 2411–2502.

[4] S. Farzad, M.A. Mandegari, J.F. Görgens, A critical review on biomass gasification, co-gasification, and their environmental assessments, Biofuel Res. J. 3 (4) (2016) 483–495.

[5] J. Artz, T.E. Müller, K. Thenert, J. Kleinekorte, R. Meys, A. Sternberg, A. Bardow, W. Leitner, Sustainable conversion of carbon dioxide: An integrated review of catalysis and life cycle assessment, Chem. Rev. 118 (2) (2018) 434–504.

[6] X. Zhang, A.O. Oyedun, A. Kumar, D. Oestreich, U. Arnold, J. Sauer, An optimized process design for oxymethylene ether production from woody-biomass-derived syngas, Biomass Bioenergy 90 (2016) 7–14.

[7] G.A. Olah, Beyond oil and gas: The methanol economy, Angew. Chem. Int. Edn 44 (18) (2005) 2636–2639.

[8] G.A. Olah, Towards oil independence through renewable methanol chemistry, Angew. Chem. Int. Edn 52 (1) (2013) 104–107.

[9] M. Mikkelsen, M. Jørgensen, F.C. Krebs, The teraton challenge. a review of fixation and transformation of carbon dioxide, Energy Environ. Sci. 3 (1) (2010) 43–81.

[10] P. De Luna, C. Hahn, D. Higgins, S.A. Jaffer, T.F. Jaramillo, E.H. Sargent, What would it take for renewably powered electrosynthesis to displace petrochemical processes? Science 364 (6438) (2019) eaav3506.

[11] G. Centi, S. Perathoner, Opportunities and prospects in the chemical recycling of carbon dioxide to fuels, Catal. Today 148 (3–4) (2009) 191–205.

[12] C. Song, Global challenges and strategies for control, conversion and utilization of CO_2 for sustainable development involving energy, catalysis, adsorption and chemical processing, Catal. Today 115 (1–4) (2006) 2–32.

[13] I.M. Dahl, S. Kolboe, On the reaction mechanism for propene formation in the MTO reaction over SAPO-34, Catal. Lett. 20 (3) (1993) 329–336.

[14] I.M. Dahl, S. Kolboe, On the reaction mechanism for hydrocarbon formation from methanol over SAPO-34: I. isotopic labeling studies of the co-reaction of ethene and methanol, J. Catal. 149 (2) (1994) 458–464.

[15] W. Song, D.M. Marcus, H. Fu, J.O. Ehresmann, J.F. Haw, An oft-studied reaction that may never have been: Direct catalytic conversion of methanol or dimethyl ether to hydrocarbons on the solid acids HZSM-5 or HSAPO-34, J. Am. Chem. Soc. 124 (15) (2002) 3844–3845.

[16] J. Amsler, P.N. Plessow, F. Studt, Effect of impurities on the initiation of the methanol-to-olefins process: Kinetic modeling based on Ab initio rate constants, Catal. Lett. (2021) 1–8.

[17] W. Wang, A. Buchholz, M. Seiler, M. Hunger, Evidence for an initiation of the methanol-to-olefin process by reactive surface methoxy groups on acidic zeolite catalysts, J. Am. Chem. Soc 125 (49) (2003) 15260–15267.

[18] A. Comas-Vives, M. Valla, C. Copéret, P. Sautet, Cooperativity between Al sites promotes hydrogen transfer and carbon–carbon bond formation upon dimethyl ether activation on alumina, ACS Cent. Sci. 1 (6) (2015) 313–319.

[19] P.N. Plessow, F. Studt, Unraveling the mechanism of the initiation reaction of the methanol to olefins process using ab initio and DFT calculations, ACS Catal. 7 (11) (2017) 7987–7994.

[20] Y. Liu, F.M. Kirchberger, S. Müller, M. Eder, M. Tonigold, M. Sanchez-Sanchez, J.A. Lercher, Critical role of formaldehyde during methanol conversion to hydrocarbons, Nature Commun. 10 (1) (2019) 1–9.

[21] X. Wu, Z. Zhang, Z. Pan, X. Zhou, A. Bodi, P. Hemberger, Ketenes in the induction of the methanol-to-olefins process, Angew. Chem. Int. Edn (2022).

[22] L. Yang, T. Yan, C. Wang, W. Dai, G. Wu, M. Hunger, W. Fan, Z. Xie, N. Guan, L. Li, Role of acetaldehyde in the roadmap from initial carbon–carbon bonds to hydrocarbons during methanol conversion, ACS Catal. 9 (7) (2019) 6491–6501.

[23] W. Chen, G. Li, X. Yi, S.J. Day, K.A. Tarach, Z. Liu, S.-B. Liu, S.C. Edman Tsang, K. Góra-Marek, A. Zheng, Molecular understanding of the catalytic consequence of ketene intermediates under confinement, J. Am. Chem. Soc. 143 (37) (2021) 15440–15452.

[24] A.D. Chowdhury, K. Houben, G.T. Whiting, M. Mokhtar, A.M. Asiri, S.A. Al-Thabaiti, S.N. Basahel, M. Baldus, B.M. Weckhuysen, Initial carbon–carbon bond formation during the early stages of the methanol-to-olefin process proven by zeolite-trapped acetate and methyl acetate, Angew. Chem. 128 (51) (2016) 16072–16077.

[25] G.J. Hutchings, R. Hunter, Hydrocarbon formation from methanol and dimethyl ether: A review of the experimental observations concerning the mechanism of formation of the primary products, Catal. Today 6 (3) (1990) 279–306.

[26] D. Lesthaeghe, V. Van Speybroeck, G.B. Marin, M. Waroquier, Understanding the failure of direct C-C coupling in the zeolite-catalyzed methanol-to-olefin process, Angew. Chem. 118 (11) (2006) 1746–1751.

[27] G.A. Olah, H. Doggweiler, J.D. Felberg, S. Frohlich, M.J. Grdina, R. Karpeles, T. Keumi, S.-i. Inaba, W.M. Ip, K. Lammertsma, et al., Onium ylide chemistry. 1. Bifunctional acid-base-catalyzed conversion of heterosubstituted methanes into ethylene and derived hydrocarbons. The onium ylide mechanism of the C_1 . C_2 conversion, J. Am. Chem. Soc. 106 (7) (1984) 2143–2149.

[28] C.D. Chang, A.J. Silvestri, The conversion of methanol and other O-compounds to hydrocarbons over zeolite catalysts, J. Catal. 47 (2) (1977) 249–259.

[29] E.A. Swabb, B.C. Gates, Diffusion, reaction, and fouling in H-mordenite crystallites. The catalytic dehydration of methanol, Ind. Eng. Chem. Fundam. 11 (4) (1972) 540–545.

[30] P. Sinclair, C. Catlow, Generation of carbenes during methanol conversion over Brønsted acidic aluminosilicates. A computational study, J. Phys. Chem. B 101 (3) (1997) 295–298.

[31] J.K. Clarke, R. Darcy, B.F. Hegarty, E. O'Donoghue, V. Amir-Ebrahimi, J.J. Rooney, Free radicals in dimethyl ether on H-ZSM-5 zeolite. a novel dimension of heterogeneous catalysis, J. Chem. Soc., Chem. Commun. (5) (1986) 425–426.

[32] N. Tajima, T. Tsuneda, F. Toyama, K. Hirao, A new mechanism for the first carbon- carbon bond formation in the MTG process: A theoretical study, J. Am. Chem. Soc 120 (32) (1998) 8222–8229.

[33] Y. Ono, T. Mori, Mechanism of methanol conversion into hydrocarbons over ZSM-5 zeolite, J. Chem. Soc., Farad. Trans. 1 77 (9) (1981) 2209–2221.

[34] J. Li, Z. Wei, Y. Chen, B. Jing, Y. He, M. Dong, H. Jiao, X. Li, Z. Qin, J. Wang, et al., A route to form initial hydrocarbon pool species in methanol conversion to olefins over zeolites, J. Catal. 317 (2014) 277–283.

[35] J.E. Jackson, F.M. Bertsch, Conversion of methanol to gasoline: New mechanism for formation of the first carbon-carbon bond, J. Am. Chem. Soc. 112 (25) (1990) 9085–9092.

[36] Z. Pan, A. Puente-Urbina, S.R. Batool, A. Bodi, X. Wu, Z. Zhang, J.A. van Bokhoven, P. Hemberger, Tuning the zeolite acidity enables selectivity control by suppressing ketene formation in lignin catalytic pyrolysis, Nature Commun. 14 (1) (2023) 4512.

[37] P.N. Plessow, A. Smith, S. Tischer, F. Studt, Identification of the reaction sequence of the MTO initiation mechanism using ab initio-based kinetics, J. Am. Chem. Soc. 141 (14) (2019) 5908–5915.

[38] W. Wang, M. Hunger, Reactivity of surface alkoxy species on acidic zeolite catalysts, Acc. Chem. Res. 41 (8) (2008) 895–904.

[39] S.R. Blaszkowski, R.A. van Santen, The mechanism of dimethyl ether formation from methanol catalyzed by zeolitic protons, J. Am. Chem. Soc 118 (21) (1996) 5152–5153.

[40] E. Sandré, M.C. Payne, J.D. Gale, First principles location of the transition state for formation of dimethyl ether in a zeolite, Chem. Commun. (22) (1998) 2445–2446.

[41] W. Wang, M. Seiler, M. Hunger, Role of surface methoxy species in the conversion of methanol to dimethyl ether on acidic zeolites investigated by in situ stopped-flow MAS NMR spectroscopy, J. Phys. Chem. B 105 (50) (2001) 12553–12558.

[42] R.T. Carr, M. Neurock, E. Iglesia, Catalytic consequences of acid strength in the conversion of methanol to dimethyl ether, J. Catal. 278 (1) (2011) 78–93.

[43] P.G. Moses, J.K. Nørskov, Methanol to dimethyl ether over ZSM-22: A periodic density functional theory study, ACS Catal. 3 (4) (2013) 735–745.

[44] A.J. Jones, E. Iglesia, Kinetic, spectroscopic, and theoretical assessment of associative and dissociative methanol dehydration routes in zeolites, Angew. Chem. 126 (45) (2014) 12373–12377.

[45] A. Ghorbanpour, J.D. Rimer, L.C. Grabow, Computational assessment of the dominant factors governing the mechanism of methanol dehydration over H-ZSM-5 with heterogeneous aluminum distribution, ACS Catal. 6 (4) (2016) 2287–2298.

[46] P. Huber, F. Studt, P.N. Plessow, Reactivity of surface lewis and brønsted acid sites in zeolite catalysis: A computational case study of DME synthesis using H-SSZ-13, J. Phys. Chem. C 126 (13) (2022) 5896–5905.

[47] X. Gong, M. Caglayan, Y. Ye, K. Liu, J. Gascon, A. Dutta Chowdhury, First-generation organic reaction intermediates in zeolite chemistry and catalysis, Chem. Rev. 122 (18) (2022) 14275–14345.

[48] C.E. Bronnimann, G.E. Maciel, Carbon-13 NMR study of methanol in HY zeolite, J. Am. Chem. Soc. 108 (23) (1986) 7154–7159.

[49] T.R. Forester, S.-T. Wong, R.F. Howe, In situ Fourier transform ir observation of methylating species in ZSM-5, J. Chem. Soc. Chem. Commun. (21) (1986) 1611–1613.

[50] T. Forester, R.F. Howe, In situ FTIR studies of methanol and dimethyl ether in ZSM-5, J. Am. Chem. Soc. 109 (17) (1987) 5076–5082.

[51] V. Bosacek, Formation of surface-bonded methoxy groups in the sorption of methanol and methyl iodide on zeolites studied by carbon-13 MAS NMR spectroscopy, J. Phys. Chem. 97 (41) (1993) 10732–10737.

[52] F. Salehirad, M.W. Anderson, Solid-state NMR studies of adsorption complexes and surface methoxy groups on methanol-sorbed microporous materials, J. Catal. 177 (2) (1998) 189–207.

[53] V. Bosáček, R. Klik, F. Genoni, G. Spano, F. Rivetti, F. Figueras, Terminal and bridging methoxyls on zeolites detected by ^{13}C magic angle spinning NMR spectroscopy, Magn. Reson. Chem. 37 (13) (1999) S135–S141.

[54] M. Seiler, U. Schenk, M. Hunger, Conversion of methanol to hydrocarbons on zeolite HZSM-5 investigated by in situ MAS NMR spectroscopy under flow conditions and on-line gas chromatography, Catal. Lett. 62 (1999) 139–145.

[55] M. Migliori, A. Aloise, E. Catizzone, G. Giordano, Kinetic analysis of methanol to dimethyl ether reaction over H-MFI catalyst, Ind. Eng. Chem. Res. 53 (38) (2014) 14885–14891.

[56] D. Masih, S. Rohani, J.N. Kondo, T. Tatsumi, Low-temperature methanol dehydration to dimethyl ether over various small-pore zeolites, Appl. Catal. B 217 (2017) 247–255.

[57] J. Nováková, L. Kubelková, K. Habersberger, Z. Dolejšek, Catalytic activity of dealuminated y and HZSM-5 zeolites measured by the temperature-programmed desorption of small amounts of preadsorbed methanol and by the low-pressure flow reaction of methanol, J. Chem. Soc. Faraday Trans. 1 80 (6) (1984) 1457–1465.

[58] J. Nováková, L. Kubelková, Z. Dolejšek, Primary reaction steps in the methanol-to-olefin transformation on zeolites, J. Catal. 108 (1) (1987) 208–213.
[59] F. Salehirad, M.W. Anderson, Solid-state13C MAS NMR study of methanol-to-hydrocarbon chemistry over H-SAPO-34, J. Catal. 164 (2) (1996) 301–314.
[60] X. Wu, M.G. Abraha, R.G. Anthony, Methanol conversion on SAPO-34: Reaction condition for fixed-bed reactor, Appl. Catal. A 260 (1) (2004) 63–69.
[61] Y. Ji, P. Gao, Z. Zhao, D. Xiao, Q. Han, H. Chen, K. Gong, K. Chen, X. Han, X. Bao, et al., Oxygenate-based routes regulate syngas conversion over oxide–zeolite bifunctional catalysts, Nat. Catal. 5 (7) (2022) 594–604.
[62] X. Chen, M.L. Neidig, R. Tuinstra, A. Malek, Direct observation of acetyl group formation from the reaction of CO with methylated H-MOR by in situ diffuse reflectance infrared spectroscopy, J. Phys. Chem. Lett. 1 (20) (2010) 3012–3015.
[63] Y. Liu, S. Müller, D. Berger, J. Jelic, K. Reuter, M. Tonigold, M. Sanchez-Sanchez, J.A. Lercher, Formation mechanism of the first carbon–carbon bond and the first olefin in the methanol conversion into hydrocarbons, Angew. Chem. 128 (19) (2016) 5817–5820.
[64] D.B. Rasmussen, J.M. Christensen, B. Temel, F. Studt, P.G. Moses, J. Rossmeisl, A. Riisager, A.D. Jensen, Ketene as a reaction intermediate in the carbonylation of dimethyl ether to methyl acetate over mordenite, Angew. Chem. Int. Edn 54 (25) (2015) 7261–7264.
[65] O. Dewaele, V.L. Geers, G.F. Froment, G.B. Marin, The conversion of methanol to olefins: A transient kinetic study, Chem. Eng. Sci. 54 (20) (1999) 4385–4395.
[66] G.J. Hutchings, F. Gottschalk, R. Hunter, Comments on" kinetic model for methanol conversion to olefins" with respect to methane formation at low conversion, Ind. Eng. Chem. Res. 26 (3) (1987) 635–637.
[67] F.M. Kirchberger, Y. Liu, P.N. Plessow, M. Tonigold, F. Studt, M. Sanchez-Sanchez, J.A. Lercher, Mechanistic differences between methanol and dimethyl ether in zeolite-catalyzed hydrocarbon synthesis, Proc. Natl. Acad. Sci. USA 119 (4) (2022) e2103840119.
[68] Z. Chen, Y. Ni, Y. Zhi, F. Wen, Z. Zhou, Y. Wei, W. Zhu, Z. Liu, Coupling of methanol and carbon monoxide over H-ZSM-5 to form aromatics, Angew. Chem. Int. Edn 57 (38) (2018) 12549–12553.
[69] P. Huber, P.N. Plessow, A computational investigation of the decomposition of acetic acid in H-SSZ-13 and its role in the initiation of the MTO process, Catal. Sci. Technol. 13 (6) (2023) 1905–1917.
[70] S. Müller, Y. Liu, M. Vishnuvarthan, X. Sun, A.C. van Veen, G.L. Haller, M. Sanchez-Sanchez, J.A. Lercher, Coke formation and deactivation pathways on H-ZSM-5 in the conversion of methanol to olefins, J. Catal. 325 (2015) 48–59.
[71] P.N. Plessow, F. Studt, Theoretical insights into the effect of the framework on the initiation mechanism of the MTO process, Catal. Lett. 148 (2018) 1246–1253.
[72] J.P. Perdew, K. Burke, M. Ernzerhof, Generalized gradient approximation made simple, Phys. Rev. Lett. 77 (18) (1996) 3865.
[73] S. Grimme, J. Antony, S. Ehrlich, H. Krieg, A consistent and accurate ab initio parametrization of density functional dispersion correction (DFT-D) for the 94 elements H-Pu, J. Chem. Phys. 132 (15) (2010) 154104.
[74] P.N. Plessow, Efficient transition state optimization of periodic structures through automated relaxed potential energy surface scans, J. Chem. Theory Comput. 14 (2) (2018) 981–990.
[75] G. Henkelman, H. Jónsson, Improved tangent estimate in the nudged elastic band method for finding minimum energy paths and saddle points, J. Chem. Phys. 113 (22) (2000) 9978–9985.
[76] G. Henkelman, H. Jónsson, A dimer method for finding saddle points on high dimensional potential surfaces using only first derivatives, J. Chem. Phys. 111 (15) (1999) 7010–7022.
[77] R.Y. Brogaard, R. Henry, Y. Schuurman, A.J. Medford, P.G. Moses, P. Beato, S. Svelle, J.K. Nørskov, U. Olsbye, Methanol-to-hydrocarbons conversion: The alkene methylation pathway, J. Catal. 314 (2014) 159–169.
[78] T.J. Goncalves, P.N. Plessow, F. Studt, On the accuracy of density functional theory in zeolite catalysis, ChemCatChem 11 (17) (2019) 4368–4376.
[79] J. Sauer, Ab initio calculations for molecule–surface interactions with chemical accuracy, Acc. Chem. Res. 52 (12) (2019) 3502–3510.
[80] C. Riplinger, P. Pinski, U. Becker, E.F. Valeev, F. Neese, Sparse maps—A systematic infrastructure for reduced-scaling electronic structure methods. II. linear scaling domain based pair natural orbital coupled cluster theory, J. Chem. Phys. 144 (2) (2016) 024109.
[81] T.H. Dunning Jr., Gaussian basis sets for use in correlated molecular calculations. I. the atoms boron through neon and hydrogen, J. Chem. Phys. 90 (2) (1989) 1007–1023.
[82] F. Weigend, R. Ahlrichs, Balanced basis sets of split valence, triple zeta valence and quadruple zeta valence quality for H to Rn: Design and assessment of accuracy, Phys. Chem. Chem. Phys. 7 (18) (2005) 3297–3305.
[83] D. Feller, Application of systematic sequences of wave functions to the water dimer, J. Chem. Phys. 96 (8) (1992) 6104–6114.
[84] T. Helgaker, W. Klopper, H. Koch, J. Noga, Basis-set convergence of correlated calculations on water, J. Chem. Phys. 106 (23) (1997) 9639–9646.
[85] G. Kresse, J. Hafner, Ab initio molecular dynamics for liquid metals, Phys. Rev. B 47 (1993) 558–561.
[86] G. Kresse, J. Hafner, Ab initio molecular-dynamics simulation of the liquid-metal–amorphous-semiconductor transition in germanium, Phys. Rev. B 49 (1994) 14251–14269.
[87] G. Kresse, J. Furthmüller, Efficiency of ab-initio total energy calculations for metals and semiconductors using a plane-wave basis set, Comput. Mater. Sci. 6 (1) (1996) 15–50.
[88] G. Kresse, J. Furthmüller, Efficient iterative schemes for ab initio total-energy calculations using a plane-wave basis set, Phys. Rev. B 54 (16) (1996) 11169.
[89] G. Kresse, D. Joubert, From ultrasoft pseudopotentials to the projector augmented-wave method, Phys. Rev. B 59 (3) (1999) 1758.
[90] A.H. Larsen, J.J. Mortensen, J. Blomqvist, I.E. Castelli, R. Christensen, M. Dułak, J. Friis, M.N. Groves, B. Hammer, C. Hargus, et al., The atomic simulation environment—a Python library for working with atoms, J. Phys.: Condens. Matter 29 (27) (2017) 273002.
[91] F. Neese, The ORCA program system, WIREs Comput. Mol. Sci. 2 (1) (2012) 73–78.
[92] F. Neese, F. Wennmohs, A. Hansen, U. Becker, Efficient, approximate and parallel Hartree–Fock and hybrid DFT calculations. a 'chain-of-spheres' algorithm for the Hartree–Fock exchange, Chem. Phys. 356 (1–3) (2009) 98–109.
[93] A development of University of Karlsruhe and Forschungszentrum Karlsruhe GmbH (1989–2007), TURBOMOLE GmbH since 2007, Turbomole V7.4.1, 2019, URL http://www.turbomole.com.
[94] K. Eichkorn, O. Treutler, H. Öhm, M. Häser, R. Ahlrichs, Auxiliary basis sets to approximate Coulomb potentials, Chem. Phys. Lett. 240 (4) (1995) 283–290.
[95] S. Kozuch, S. Shaik, How to conceptualize catalytic cycles? The energetic span model, Acc. Chem. Res. 44 (2) (2011) 101–110.
[96] T. James, C. Wellington, Thermal decomposition of β-propiolactone in the gas phases, J. Am. Chem. Soc. 91 (27) (1969) 7743–7746.
[97] P.N. Plessow, F. Studt, Olefin methylation and cracking reactions in H-SSZ-13 investigated with ab initio and DFT calculations, Catal. Sci. Technol. 8 (17) (2018) 4420–4429.